Simultaneously enhanced photon absorption and charge transport on a distorted graphitic carbon nitride toward visible light photocatalytic activity

Zhou Chen, Tingting Fan, Mengyi Shao, Xiang Yu, Qiuling Wu, Jianhui Li, Weiping Fang, Xiaodong Yi*

National Engineering Laboratory for Green Chemical Productions of Alcohols, Ethers and Esters, College of Chemistry and Chemical Engineering, Xiamen University, Xiamen 361005, PR China

ABSTRACT

The graphitic carbon nitride (g-C$_3$N$_4$) has emerged as one of the most promising candidates to replace the metal oxide-based catalysts for highly efficient photocatalytic materials. However, the intrinsic drawbacks of weak visible-light adsorption and poor charge separation efficiency seriously limit its practical applications. Thus, struggling controls over their structure parameters to optimize the photoelectrical properties on molecular-level for realizing highly active metal-free g-C$_3$N$_4$ photocatalysts have attracted a lot of focuses. Herein, a novel isopropanol assisted solvothermal-copolymerization strategy is rationally designed to synthesize a compact O, S-co-doping g-C$_3$N$_4$ (CNUS) with markedly reinforced π-π* and n-π* electron transitions. The meliorative structure and energy level configuration result in elevated effects for both visible-light (photon) adsorption and photo-induced carries transfer, and the CNUS exhibits outstanding photocatalytic hydrogen evolution and rhodamine B degradation performance under visible light. In addition, after continuously testing, the CNUS still shows superior stability with nearly negligible decay for both photocatalytic reactions. The characterization results indicate that the incorporated oxygen and sulfur engineer the charge, and the layered-stacking distance decreases from 0.328 to 0.322 nm, compared its counterpart (CNU prepared by direct pyrolysis of urea). Importantly, the enriched charge facilitates the rate-limiting separation of photogenerated carriers, and hence improved the visible light photocatalytic efficiency.

1. Introduction

The development of both photocatalytic water splitting technology and organic contaminant degradation to solve the energy shortage and environment pollution problems relies heavily on design of photocatalysts, including oxides, sulfides, organic polymers and their composites [1–4]. Headed by Wang et al [5], the graphitic carbon nitride (g-C$_3$N$_4$) have been well developed and used as an awakening photocatalyst. They are now widely applied in many photocatalytic areas, including photo-driven water splitting [6–8], CO$_2$ reduction [9–12], organic contaminant degradation [13,14], and bioimaging [15], owing to the virtue of their suitable highest occupied molecular orbital (HOMO) and lowest unoccupied molecular orbital (LUMO) positions, earth-abundance, robust stability, and easy tunable structure. However, the sluggish exciton dissociation, insufficient active sites, faster recombination of photogenerated carriers and weak visible light absorption of g-C$_3$N$_4$ originating from the direct pyrolysis of isolated nitrogen-rich molecular precursors (usually, they are melamine, urea,

cyanamide, and dicyandiamide.) at high temperature greatly hinder their photoactivity [16–18]. Thus, continuing efforts have been focused on establishing g-C$_3$N$_4$ with different morphology and dimensionality and constructing heterojunction with suitable semiconductors [16,19–28], which inevitably increase the costs of materials and processing.

Actually, it has been reported that the optical and electronic properties of g-C$_3$N$_4$ framework can be readily tuned by P doping, in which the additional midgap energy level plays a stimulant role in determining visible absorption and charge transfer efficiency of g-C$_3$N$_4$, and thus can modify its visible-light-driven photocatalytic performance [29]. In addition, engineering C-ring and nitrogen vacancies on g-C$_3$N$_4$ also occupy essential roles in tuning the band gap structure, extending the light absorption, increasing the charge transfer mobility, and creating more active sites for realizing considerable photocatalytic activities [30–32]. For example, Che et al [32]. reported that a local in-plane π-conjugated electric field formed between the carbon ring and the g-C$_3$N$_4$ plane heterostructural nanosheet can synergistically

---

elongate the photocarrier diffusion length and lifetime. In addition, the homogeneous self-modified nitrogen vacancies on g-C$_3$N$_4$ manipulated under hydrogen atmosphere have a widened visible light absorption range, and can suppress radiative recombination of photo-excited charge carriers [30]. Other efforts have been made to fabricate surface transient state metal co-catalysts, such as Ni$_x$P$_y$ [33,34], NiS$_x$ [35,36], Co-based [37,38], and Mo-based [39,40] etc., which ignore the lower bond interaction between organic and inorganic interfaces, and thus not conducive to the charge transfer in some extent [41]. Therefore, there are still plenty of spaces to explore new fundamental approaches besides currently multifunctional strategies.

Recently, both theoretical calculations and experiments have demonstrated that distorted g-C$_3$N$_4$ structure can promote additional n-π* transitions of optical absorption [42]. The basic units and connecting mode of g-C$_3$N$_4$ have no major alternation, but the charge separation is drastically promoted due to the two-dimension (2D) corrugated structure with higher degree of polycondensation. Importantly, its wavelength-dependent activity can be extended to 550 nm with desirable H$_2$ production. To date, only a few studies have been concentrated on designing distorted g-C$_3$N$_4$ for synchronous enhanced π-π* and n-π* electron transitions. For instance, a highly crystalline g-C$_3$N$_4$ with a 0.292 nm π-π* layer stacking distance of heptazine units was synthesized by a tandem method that firstly co-condensation of urea and oxamide and followed by post-calcination in molten salt. As a result, it decreases the optical band gap, and improves the lateral charge transport and interlayer exciton dissociation of g-C$_3$N$_4$ [43,44]. Analogously, a well crystallized g-C$_3$N$_4$ with improved visible-light-driven photoactivity was fabricated by a simply polymerization of dicyandiamide in a closed stainless steel autoclave [45]. Here, the closed stainless steel autoclave was used to afford a high pressure reaction environment. The compacted layered stacking distance enhanced the charge transfer, and the damaged hydrogen bonds in C−N covalent bonds-dominated intralayer framework broadened the light-responsive range of carbon nitride. This is can be explained by the facilitating n-π* electron transition involving the lone pairs of the edge nitrogen atoms in the heptazine units. However, extra acid or molten salt additives and difficult post-handling conditions make each of these talented strategies more complex.

Herein, for the first time, a simple, environmentally friendly and scalable method to synthesize distorted g-C$_3$N$_4$ by a combination of solvothermal and pyrolysis is proposed. The as-synthesized sulfur and oxygen co-doped g-C$_3$N$_4$ (CNUS) exhibits an improved visible-light-driven H$_2$-production and rhodamine B (RhB) degradation activity. This work demonstrates a new pathway for constructing the distorted CN-based materials, which will simultaneously advance the visible light photon absorption and charge carrier transition ability, thus achieve sufficient visible light activity.

2. Results and discussion

2.1. Cross-linking network

Based on our design, the distorted g-C$_3$N$_4$ (CNUS) with sulfur and oxygen co-dopant structure is synthesized by a solvothermal-cross linking-copolymerization strategy as depicted schematically in Fig. 1a. As shown in Fig. S1, the cross-linking network with brown color is easy generated by forming hydrogen bonding between the rich lone-pair electrons at the edge of urea, thiourea and the abundant hydroxyl groups of isopropanol during solvothermal process [42]. However, the isopropanol with hydrophobic alkyl group on the surface of cross-linking network confines the further connection with other molecule in some extent, which results in an unbalanced cross-linking network. Further, the meliorative structure will realize by the sp^2-hybridized C−N bonds between the sulfur and oxygen-contained cross-linking network through partial dehydration reaction under 550 °C. It has been reported that O doping and S doping can regulate the light absorption

and energy band of C$_3$N$_4$ which will realize the enhanced visible light absorption efficiency. These results were reasonable because the doped O or S atoms influenced the distribution of C and N atoms in the lattice, leading to a hybrid of p orbitals among C, N, and O (or S) atoms. In addition, owing to the existence of the impurity level, the value of E$_{max}$ (the maximum energy gap in the band gap) was decreased, and the Fermi level was pushed just under the bottom of CB, which means that the photogenerated electron can easily jump from the impure state to the CB or from the VB to the impure state. Importantly, it was found that the role of isopropanol is very important for the synthesis of the enhanced visible light absorption g-C$_3$N$_4$. Only yellow color g-C$_3$N$_4$ can be obtained when the same amount water was used to substitute the isopropanol. This is confirmed on the other hand that this solvothermal process proposed here is crucial step to realize the enhanced photon absorption.

2.2. Oxygen and sulfur co-doping

The as-synthesized CNUS incorporated with sulfur and oxygen heterostructure can be verified by the element analysis, XPS, transmission electron microscopy (TEM) and the corresponding element mapping. The overall morphology of CNUS constitutes by well-defined porous structures and uniform size distributions, unlike the awkward morphology of CNM (melamine as precursor) but similar to CNU (urea as precursor) (Fig. S2), resulting from the release of bubble during polycondensation. However, the cross-linking network limits the generation of abundant gas during pyrolysis process, and thus leads to a lower specific surface area of CNUS (19.0 m^2 g^{-1}) than the CNU (50.8 m^2 g^{-1}), but still higher than the CNM (8.3 m^2 g^{-1}) (Fig. S3). As further confirmed by the TEM images, the homogeneous polyporous CNUS (Fig. 1e,f) is observed. Expectedly, the significant changes in the percentage of nitrogen from 58.7% for the CNU to 52.2% for the CNUS are obtained (Fig. S4). This result highly agrees with the percentage determined by X-ray photoelectron spectroscopy (XPS) (Table S1).

Both experimental and theoretical results have uncovered that the O atoms can incorporate into the g-C$_3$N$_4$ lattice by replacing the C−N═C coordinated N atoms to form C−O−C bonds [46]. Additional C−O bond (285.9 eV) in the heterocycles originated from the partial condensation of the cross-linking network is appeared in the CNUS, meaning the successful incorporation of oxygen into g-C$_3$N$_4$ (Fig. 1b). This is further confirmed by the more intense O 1 s spectrum in Fig. 1c. In addition, a newly formed S 2 p spectrum in CNUS is observed in Fig. 1d. However, according to the results of element analysis, the content of sulfur in CNUS is extremely lower than oxygen (Fig. S4). The XPS peak at around 169.1 eV corresponds to the presence of sulfite species [47] such as SO$_3^{2-}$ and SO$_4^{2-}$ on the surface due to the co-doping of O and S in the structure. The sulfite species could be easily formed due to the presence of oxygen during the pyrolysis step. In addition, it should be noticed that a slightly weak peak at around 163.9 eV belonging to the S−C chemical bonds also can be observed in the Fig. 1d.

The plausible reason for the lower contents of S is that the major role of the S species is mediated the synthesis, and it is difficult for sulfur species to incorporate in the carbon nitride semiconductors [48]. The presence of sulfur motifs can provide an extra chemical way to control the polymerization due to the involvement of easy leaving groups (such as −SH) under air conditions, as elucidated by Zhang et al [48]. On the other hand, It is easier to develop an oxygen-doped g-C$_3$N$_4$, considering that oxygen atom possesses atomic radii similar to C or N atoms [49]. Therefore, although the amount of thiourea in the synthesis precursor is the same as urea, the content of oxygen in the urea together with the hydroxyl provided by isopropanol results in drastically higher oxygen content in the CNUS than sulfur species, as explained by the element analysis and XPS results.

In addition, the reduction of hydrogen content in CNUS is because of the break of the edge hydrogen bonds, meaning that the localized electronic hybridization of edge sites of the polymers are reconstructed.
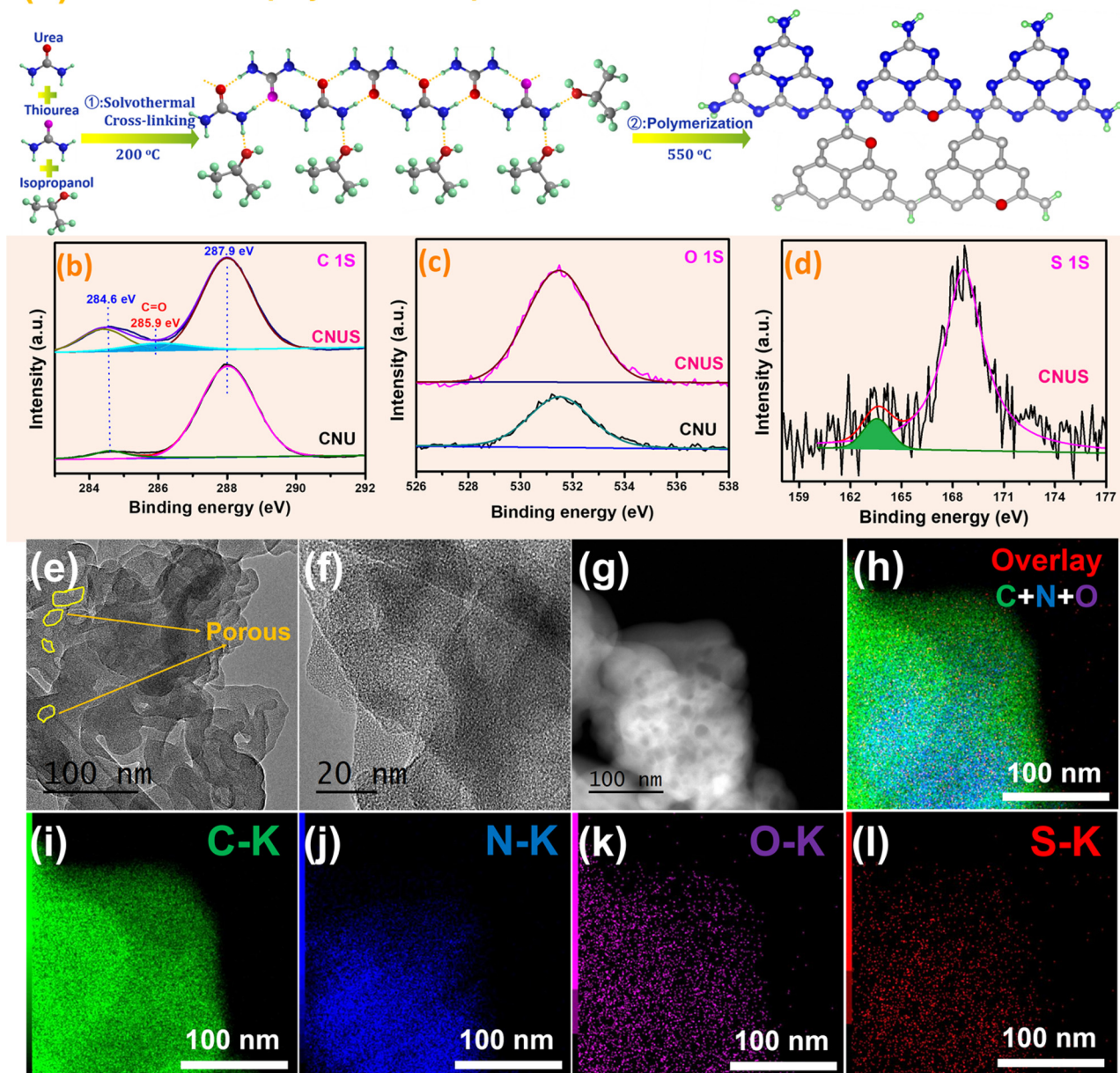
Fig. 1. (a) Synthetic route of CNUS by solvothermal-polymerization process, (b) C 1 s, (c) O 1 s and (d) S 2p XPS spectra of CNU and CNUS, (e, f) transmission electron microscope (TEM) image, (g) high angle annular dark field (HAADF), (h) the corresponding overlay element mapping of C, N, O, (i) C, (j) N, (k) O and (l) S of CNUS.

The carbon and nitrogen bonding compositions, C/N ratio and percentage of nitrogen of CNU and CNUS are listed in the Table S1. The high-angle annular dark-field scanning transmission electron microscopy (HAADF) and the corresponding elemental mappings (Fig. 1g–l) reveal that the C, N, O and S are homogeneously distributed over the entire sample. The important role of S species during synthesis process can be further confirmed by our contrast experiments. As shown in Fig. S5 and S6, different ratio of urea and thiourea was synthesized by the same method. The CNUS (CNUS-2 in Fig. S5 and S6 is the same as CNUS) shows the best visible light absorption and the best photocatalytic degradation activity of RhB. It should be emphasized that without adding thiourea, only a white intermediate and faint yellow g-C_3N_4 can be obtained, and there are only little product under further polymerization process. According to the above contrast experiments, it should be emphasized that the sulfur species coming from thiourea is an essential part in this synthesis strategy. Therefore, it can be concluded

that the oxygen and sulfur are successfully substituted on the heptazine units to form C−O, S−C and S−O bonds, which is highly dependent on our proposed oxygen and sulfur co-doping cross-linking network. Next, we focus on exploring the relationship between the structure and the photocatalytic performance of CNUS.

2.3. Distorted structure

Since the electronegativity of oxygen (3.44) is higher than nitrogen (3.04), and the atomic radius of S (104 pm) is higher than carbon (77 pm) and nitrogen (70 pm), the adulteration of oxygen and sulfur will result in the unbalanced plane. The interaction between the interlayers can be strengthened by powerful van der Waals' force, resulting in a distorted structure of CNUS. Importantly, an oxygen atom or sulfur has one more free electron than a nitrogen atom and the exposure of free oxygen and sulfur atoms realizes the n-π* electron
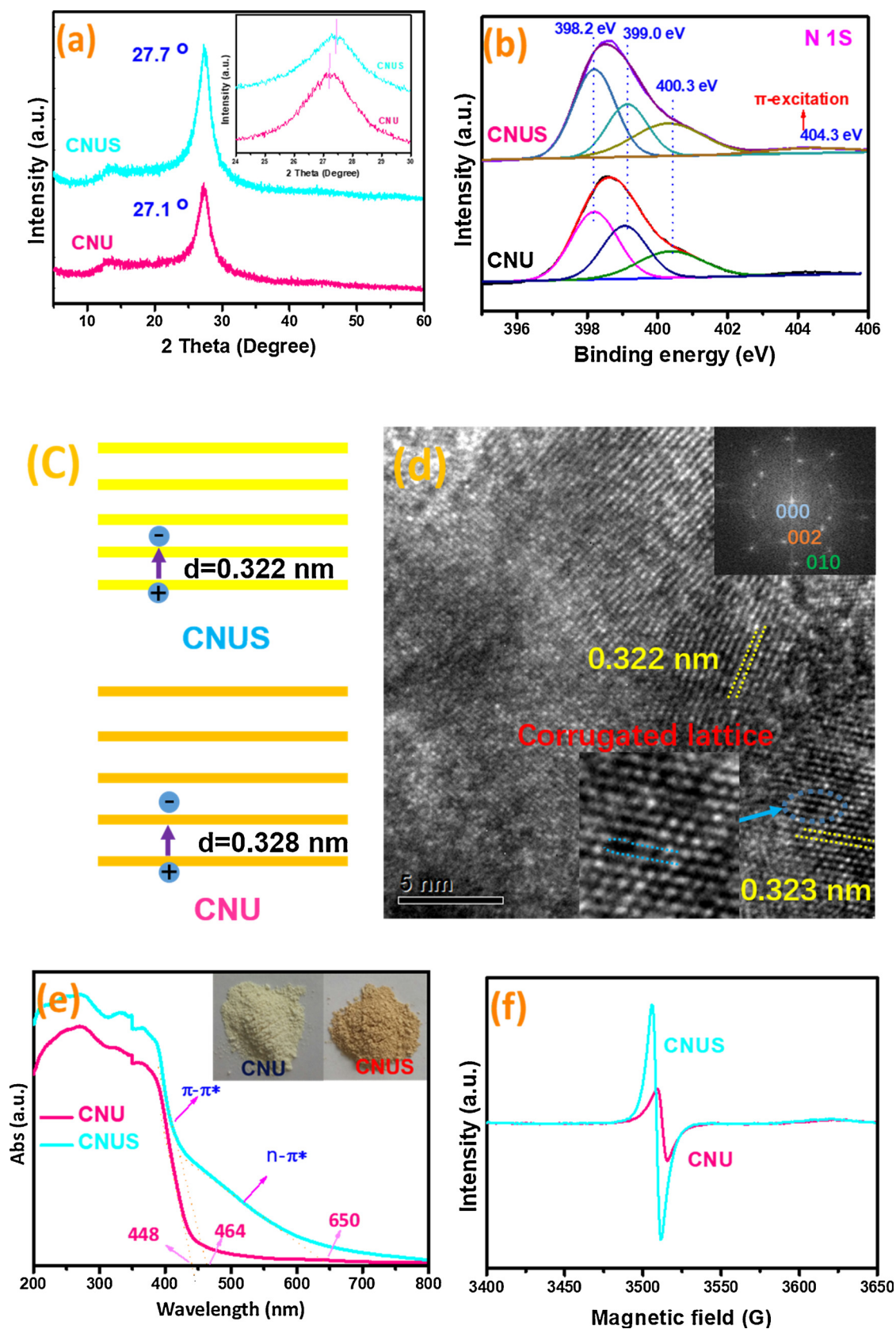
Fig. 2. (a) XRD patterns, (b) N 1 s XPS spectra, (c) average interlayers instance of CNU and CNUS; (d) HRTEM image of CNUS and FFT patterns on the inset revealing the higher crystallinity and distorted of CNUS; (e) DRS spectra (inset is the optical photogragh), (b) electron spin resonance (ESR) signals of CNU and CNUS.

transition, implying the generation of an asymmetric planar structure for the CNUS. Absolutely, this distorted structure will indirectly lead a compacted interlayers staking [42,45]. The powder X-Ray Diffraction (XRD), high resolution transmission electron microscopy (HRTEM) and Fourier transform infrared spectrum (FT-IR) technologies are carried to confirm this.

Firstly, the XRD pattern (Fig. 2a) of CNUS prepared by isopropanol assisted solvothermal-copolymerization method shows the peaks at 12.8° (100) and 27.7° (002), corresponding to the in-plane repeated units and the interlayer stacking reflection in g-C$_3$N$_4$, respectively, which indicates that the original g-C$_3$N$_4$ crystal structure is well-maintained. However, the (002) peak of CNUS is shifted up from 27.1° of CNU to 27.7°. The main reason for this phenomenon is that the interlayer stacking distance is compacted from 0.328 nm for CNU to 0.322 nm for CNUS (the simulative renderings are depicted in Fig. 2c), which is induced by a strong van der Waals attraction between the neighboring heptazine layers.

Secondly, the XPS survey is performed to gain insight into the surface chemical states and bonding configuration information which highly related to the local environment of basic heptazine units. Both pristine CNU and CNUS exhibit quite similar C 1 s (Fig. 1b) and N 1 s (Fig. 2b) spectra, implying that the sp^2 hybridized heptazine units are hardly changed after modification of the interlayers stacking distance. The C 1 s spectra display two obvious peaks with binding energies of 284.6 eV and 287.9 eV ascribed to the sp^2-hybridized C−C bonds and the sp^2-hybridized C in aromatic skeleton rings [50], respectively. The N 1 s spectra (Fig. 2b) of two samples can be featured by three secondary peaks centered at three binding energy, 398.2 eV, 399.0 eV, and 400.3 eV, corresponding to the sp^2-hybridized pyridinic−N species in triazine rings (C−N=C), the tertiary nitrogen (N−(C)$_3$ groups), and the terminal amino groups (−N−H)) of the general g-C$_3$N$_4$ structure, respectively [16,31,51,52]. It is worth noting that a peak at 404.3 eV arisen from the charge effects or positive charge localization in the heterocycles is emerged in the CNUS, indicating that the doping of oxygen and sulfur, redistribution of local electronic [53], and slight change of interlayer stacking distance will cause a different surface chemical states in CNUS [49]. It should be mentioned that the sample synthesized by urea and isopropanol under our strategy shows the similar XPS peaks with CNUS. Compared to the XPS results of CNU, the newly formation of C−O bond and π-excitation in CNUS-0 shown in Fig. S7, further confirmed that the redistribution of local electronic can be realized by our AIP-assisted strategy.

Thirdly, as shown in Fig. S8, the peaks at 810 cm^{-1}, 1200–1700 cm^{-1} region and the broad peak ranging from 3200 to 3400 cm^{-1} are stemmed from the breathing vibration of the intrinsic heptazine units, typical C−N heterocyclic stretches of the triazine (C$_6$N$_7$) ring, and the N−H and O−H components, respectively [54,55]. Compared with the pristine CNU, the peak at 810 cm^{-1} shifts toward higher frequency by the co-condensation cross-linking network of urea, thiourea and isopropanol, suggesting the enhanced crystallinity of CNUS [31]. The highly crystalline structure of CNUS can be further verified by the HRTEM and Fast Fourier Transform (FFT) pattern. Its FFT pattern (inset in Fig. 2d) shows typical (002) diffraction for graphite stacking [56,57]. The crystal lattice of these lattice fringes shows distinct interplanar spacing of 0.323 nm and 0.322 nm, as marked in Fig. 2d, corresponding to the (002) plane of g-C$_3$N$_4$. Specially, a tortile lattice is observed in the enlarged area which induce a change in stacking distance. These characterization results reveal that the cross-linking network can act as a transition to effectively optimize the crystal structure of g-C$_3$N$_4$.

As a result, it can be speculated that the distorted structure with different surface properties will lead a much different photoelectrical properties of CNUS. We initially carry out a UV-vis diffuse reflectance spectra (DRS) test to compare the light-harvesting capability of the CNU and CNUS. It can be clearly seen that the above microstructure modification in nanoscale (especially for the higher electronegativity of O

atoms on the heptazine units) caused by distorted stacking has a notable enhanced optical absorption whatever in UV and visible light regions in comparison with the CNU (Fig. 2e), which can be verified by the color changing from yellow to brown. These results are highly agreed with the experimental and theoretical forecasts by Chen et al [42]. The intrinsic absorption bands below 450 nm are a result of π-π* electron transitions of the sp^2 hybridized C and N in the conjugated aromatic system [58]. The improved absorptive ability in the UV region reflects that the reinforced π-π* electron transition in the conjugated aromatic ring system is clearly red-shifted to the visible light region from 448 nm (CNU) to 464 nm (CNUS) due to the tighter and better packing of the joint heptazine system of CNUS. Moreover, newly emerged absorption bands from 450 nm to 800 nm are probably assigned to the n-π* electron transitions involving the lone pairs on the edge atoms (probable oxygen and sulfur in our case) of the heptazine units [42,43,59].

It is worthy to be noted that the n-π* transitions are spatially forbidden for perfectly symmetric and planar units. However, in the present study, the AIP-assisted solvothermal and copolymerization strategy enhances the interaction between the neighboring melon strands induced by charged/polarized planar units, which results in compacted interlayer stacking and allows access to this electron transition. The exposure of free oxygen atoms on the sacrifice of hydrogen bonds realizes the n-π* electron transition, implying the generation of an asymmetric planar structure for the CNUS. As evidenced in Fig. 2f, both samples exhibit an ESR signal with a g value of 2.003 attributed to an unpaired electron on the sp^2-carbon atoms of the aromatic rings within π-bonded nanosized clusters [60]. The enhanced spin intensity of CNUS is well established that the essentially promoted formation of unpaired electrons [8,61]. This is mainly due to the fact that the production of extra electrons are delocalized among the big π bonds of the g-C$_3$N$_4$. It can be explained by that the functional oxygen on the CNUS may offer extra electrons because of an oxygen atom has one more electron than a nitrogen atom. As results, these extra electrons can be redistributed to the nearest carbon atoms, resulting in delocalization of π-electrons in the conjugated heterocyclic ring of CNUS, which is confirmed by the results of XPS [26].

The creation of new absorption bands for CNUS sharply improve the light responsive range, and can be utilized for the photochemistry of visible light with wavelengths longer than 420 nm. An important feature of the absorption spectrum of CNUS is the presence of a strong tail absorption (midgap state coming from the substitution of oxygen and sulfur) in the visible region. Therefore, we show a direct consequence of molecular engineering of g-C$_3$N$_4$, which will potentially simultaneously advance the visible light photon absorption and charge carrier transition ability, thus achieve sufficient visible light activity, such as the photocatalytic hydrogen generation and the RhB degradation.

2.4. Photocatalytic performance

Next, both visible light (λ > 420 nm) photocatalytic H$_2$-production and RhB degradation activities are investigated to explore the relationship between the distorted structure and the photocatalytic performance of g-C$_3$N$_4$. As shown in Fig. 3a, with 3 wt% Pt as co-catalysts, the CNUS photocatalyst shows the highest photocatalytic H$_2$-production activity of 109.3 μmol h^{-1}, which is 59.6 times of the CNM (1.8 μmol h^{-1}), and even 6.8 times of the CNU (16.1 μmol h^{-1}). A uniform distributed Pt nanoparticles with average diameter of 3 nm are observed on the surface of CNUS, as shown in Fig. S9. It should be mentioned that the photocatalytic hydrogen generation activity achieving here is comparable to the state-of-the-art catalysts, as listed in the Table. S2. Importantly, no noticeable deterioration of stability activity is observed after three cycles test (Fig. 3b), indicating the robustness of CNUS photocatalyst, as further confirmed by the nearly unchanged XRD patterns of the fresh and used CNUS (Fig. S10).

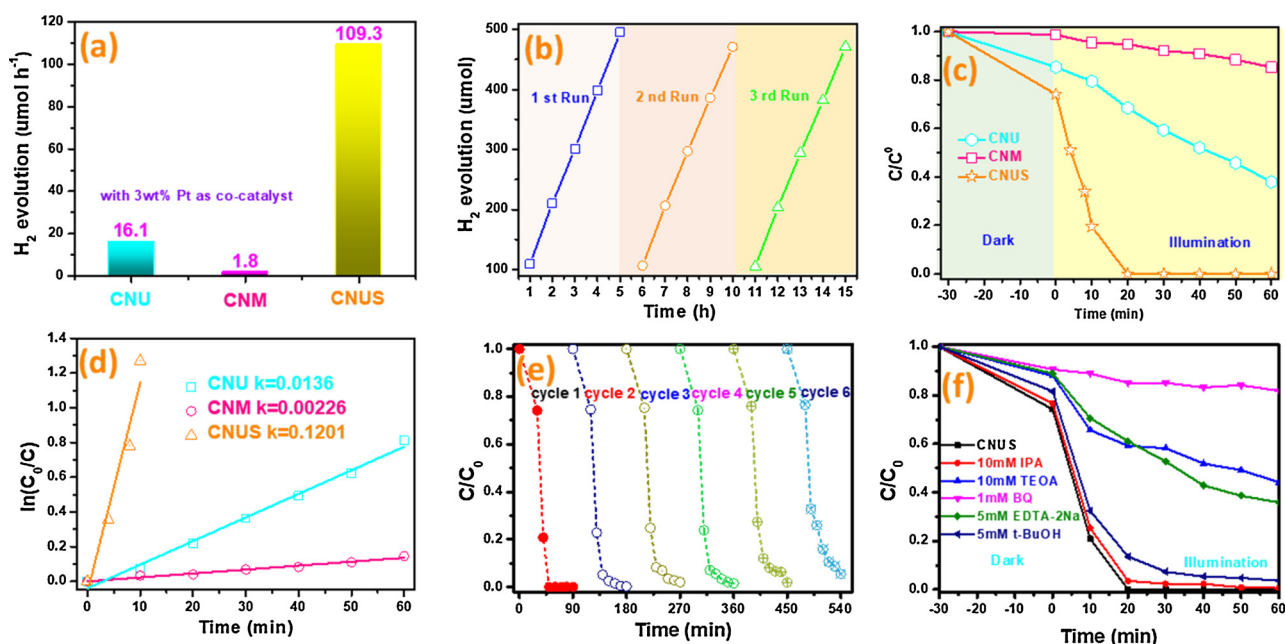The Fig. 3c, d and S11 show the results of RhB degradation under

Fig. 3. (a) H_2 generation rate over CNU, CNM and CNUS photocatalysts (300 W Xe lamp, 30 mg catalyst, 3 wt% Pt as co-catalysts, 35 ml aqueous triethanolamine solution (10 vol%)), (b) recycle of H_2 evolution of CNUS photocatalyst, (c) photocatalytic degradation activity and (d) rate of RhB ($C_0 = 10\,mg\,mL^{-1}$) over CNU, CNM and CNUS; (e) stability test of CNUS for six cycles of photocatalytic RhB degradation; (f) effect of the capture agents on the photocatalytic activity of CNUS.

visible light irradiation. The CNUS has the best degradation rate, and degrades 100% within 20 min. In contrast, the CNM and CNU degrade 10% and 30%, respectively, in 20 min. A first-order kinetics rule, that is, $\ln(C_0/C) = kt$, is used to calculated the RhB degradation rate over these three samples, where the C_0 and C are the concentration at origination, and the concentration at time t for RhB, k is the degradation reaction rate constant, respectively. The degradation rate for CNUS is 9.33 times and 56.1 times of CNU and CNM, respectively (Fig. 3d). More importantly, no noticeable deterioration of stability activity is observed after six cycles test (Fig. 3e). Compared with recent works listed in Table S3, the CNUS shows one of the most effective g-C₃N₄ materials for photocatalytic RhB degradation. Here, we can conclude that the distorted CNUS has better photocatalytic performance for both hydrogen generation and RhB degradation.

In order to further study the photocatalytic reaction mechanism and active species for the RhB degradation, some active species capture experiments are performed (Fig. 3f). The isopropanol (IPA, 10 mM), triethanolamine (TEOA, 10 mM) and parabenzoquinone (BQ, 1 mM) are used as the capture agents for ·OH, h⁺, and ·O₂⁻, respectively. There is no significant effect on the photocatalytic activity as the IPA added into the photocatalytic degradation system, indicating ·OH is not the reactive oxidation specie in this reaction [62]. In contrast, the photocatalytic degradation performance decreases apparently when the TEOA and BQ are added to the solution. However, the inhibition of photocatalytic degradation rate after the addition of TEOA is not as effective as the BQ. Further, the ehylenediaminetetraacetic acid disodium salt (EDTA-2Na, 5 mM) and tert-butanol (t-BuOH, 5 mM) are used as capture agents for h⁺ and ·OH, and the results are further compared to the active substance [63,64]. As shown in Fig. 3f, the t-BuOH shows nearly no influence for the RhB degradation performance on CNUS and EDTA-2Na exhibits similar influence extent to the IPA. Therefore, the main active substance for CNUS in photocatalytic process for RhB degradation is ·O₂⁻, and the secondary active substance is h⁺.

2.5. Photochemical properties

Since the surface area of CNUS is significantly lower than the CNU,

it indicates that the enhanced photoactivity for both photocatalytic hydrogen generation and RhB degradation are not only related to the active sites exposed, but also determined by the ability of light absorption and photogenerated carries separation. It is well known that the light-harvesting capability, and the separation and transfer rate of photogenerated charge carries of photocatalyst are very important to the photocatalytic activity.

For further exploring the possible photocatalytic mechanism on CNUS, the Kubelka-Munk method is used to calculate the band gap energy. As shown in Fig. 4a, the new midgap state energy (E_d = 2.37 eV) originating from the impurity from the HOMO to the midgap state for the CNUS is deduced. The presence of such midgap states has also been reported in the titanium oxide [65] and Bi-doped zinc sulfide [66], due to the location of electronic states within the band gap. In our case, the midgap state energy is mainly stemmed from the oxygen doping. According to the valence band (VB) XPS spectra (Fig. 4b), the positions of the valence band (VB) edge maxima are estimated to be 1.71 and 1.61 eV for CNU and CNUS, respectively. According to the former studies, the reconstruction of pi-conjugated electrons evidently induces the up-shift of valance band energy [67,68].

Combined with the band gap energy and VB energy, the electronic band structures of both samples are schematically given in Fig. 4c. Obviously, the CNUS with a midgap shows enhanced visible light absorption and better reductive reaction abilities such as hydrogen evolution. In addition, it should be mentioned that the compacted stacking (the result of distorted structure) of CNUS not only can enhance the absorption of photons with energies lower than the pristine one, but also improve the carries-separation capability [43,44]. As shown in Fig. 4d, the strong emission peak at 448 nm originates from the band-to-band recombination of the electrons and holes. However, the meliorative energy level configuration and the slightly compacted stacking construction lead to the substantial suppression of radiative charge carrier recombination in the CNUS, as indicated by the dramatically weakened PL intensities.

With the anticipation of considering that a longer charge carrier lifetime usually represents a higher possibility of participation in the photocatalytic reactions, it plays a pivotal role in determining their photocatalytic activity. The time-resolved photoluminescence (TRPL)
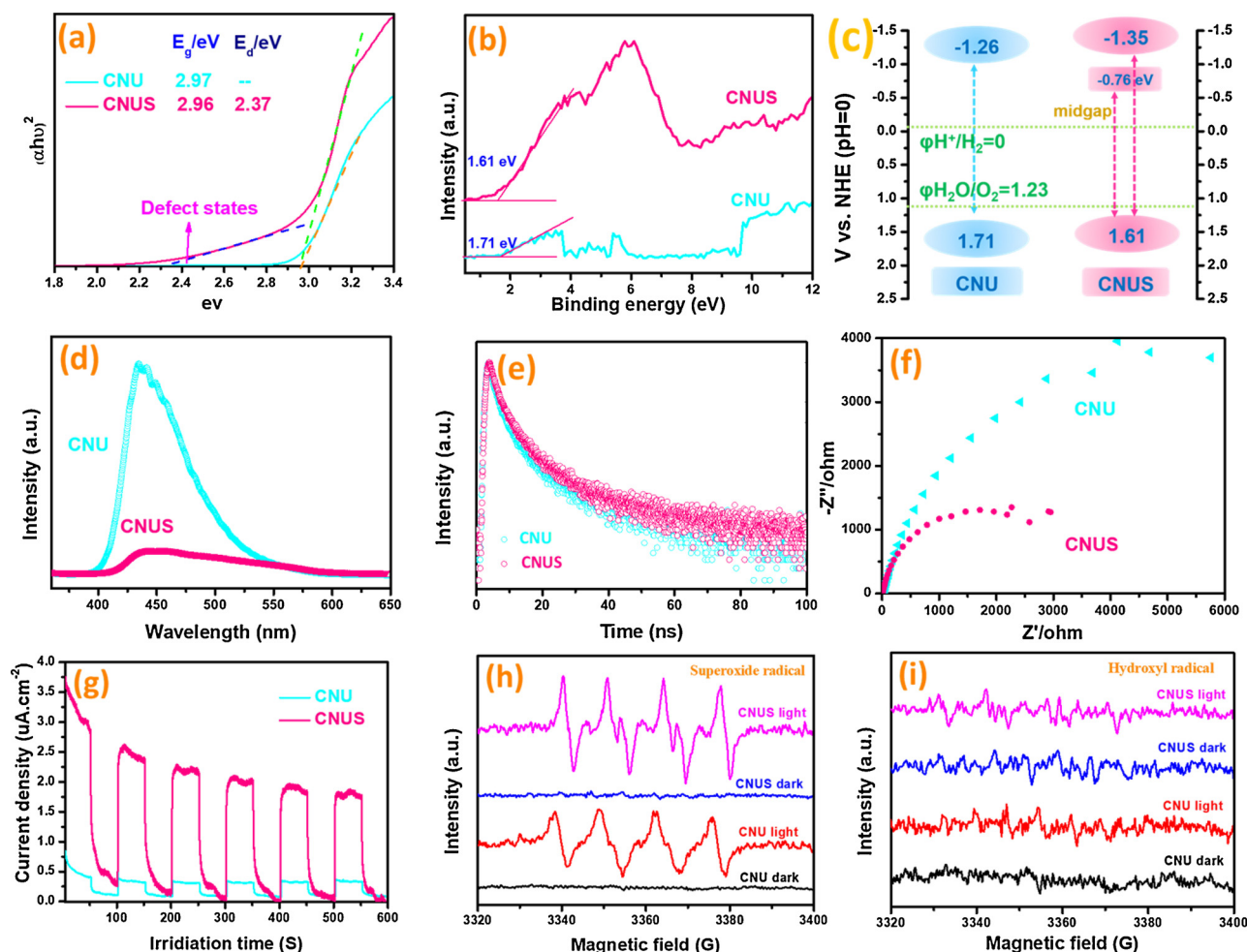
Fig. 4. (a) Kubelka-Munk transformed reflectance spectra, (b) VB XPS spectra, (c) electronic band structure, (d) photoluminescence emission spectra, (e) time-resolved PL decay spectra at λ_{ex} = 378 nm, (f) Nyquist plots of the impedance spectra, (g) transient photocurrent recorded under visible irradiation of CNU and CNUS photocatalysts. (h) Superoxide radical test in methanol and (i) hydroxyl radical test in aqueous with DMPO as radical trapper at dark and visible light conditions.

decay spectra are further carried out to investigate the photo-induced charge carrier lifetime of both photocatalysts, shown in Table S4 and Fig. 4e. Compared to the CNU, the CNUS shows an increased t_3 (39.01 ns) and t (27.04 ns) PL lifetimes, suggesting that the distorted CNUS photocatalyst can effectively elongate the lifetime of charge carriers. The longer lifetime may be attributed to the delocalization of photoexcited electrons on surface terminal sites introduced from oxygen doping distorted structure, and typically, this is beneficial for photocatalytic reaction. Therefore, the above fitting data powerfully corroborate that the lifetimes of charge carriers in CNUS are synergistically lengthened by our AIP-assisted strategy.

The huge advantage of CNUS in meliorative electronic properties could also be evaluated by electrochemical impedance spectra (EIS) and transient generation of photocurrent. With EIS analysis (Fig. 4f), it is clearly observed that the distorted CNUS present much smaller arc radius than the pristine CNU due to the narrowed interlayer distance, which means the CNUS has much lower electron-transfer resistance and higher charge transfer efficiency [69]. The increased transient photocurrent on the compacted stacking obviously implies the enhancement of exciton dissociation, and only the very fast charge pairs can recombine, further illustrating a favorable charge carrier behavior. As shown in Fig. 4g, the higher photocurrent for CNUS photocatalyst reveals more favorable photocatalytic kinetics for the photocatalytic hydrogen evolution and RhB degradation. This can be explained by the shortened layer distance in CNUS which will accelerate the charge transfer over the interlayers, promote the excitons to migration from

bulk to interface with restraining recombination, and finally act as photo-catalytic sites for proton and RhB reduction. Together, the photoelectric properties analyzed above clearly suggest that the AIP-assisted method is a highly efficient strategy for promoting the light-harvesting capability and charge separation efficiency, which is certainly favorable to enhance a better photocatalytic activity.

2.6. Possible photocatalytic mechanism

It is widely accepted that four consecutive steps are included in various photocatalytic reactions as follows: (1) light absorption; (2) photoexcitation to produce electron-hole pairs; (3) separation and migration of electron-hole pairs to surface; (4) adsorption and redox reaction on the surface active sites [70,71]. On the basis of the above experimental and characterization results, it is conceivable that the CNUS possesses with the following two features may show significantly enhanced photocatalytic hydrogen evolution and RhB degradation activity: (i) a compacted structure with midgap band enhances the π-π* and n-π* electron transitions, and (ii) oxygen-containing electron transport channel endows a long excited state lifetime. Under visible light irradiation to CNUS, the dominating reactions involved in photocatalytic process are listed in below:
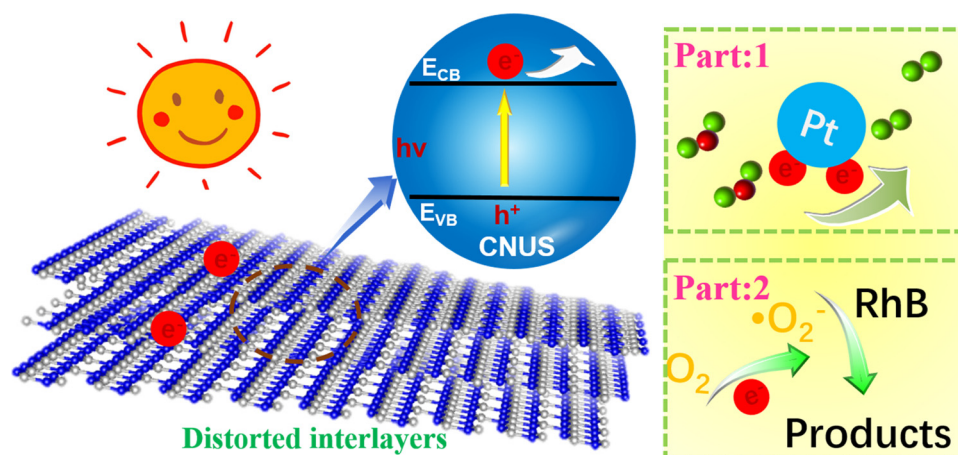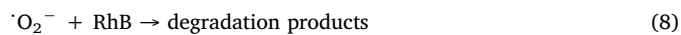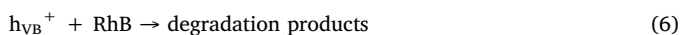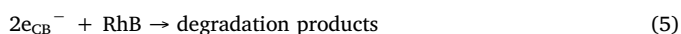
$$CNUS + h\nu \rightarrow e_{CB}^- + h_{VB}^+ \tag{1}$$

$$h_{VB}^+ + TEOA \rightarrow TEOA^+ \tag{2}$$

Fig. 5. Proposed photocatalytic mechanism on CNUS photocatalyst.

$$2e_{CB}^- + 2H^+ \rightarrow H_2 \tag{3}$$

$$h_{VB}^+ + OH^- \rightarrow {}^{\cdot}OH \tag{4}$$

$$2e_{CB}^- + RhB \rightarrow \text{degradation products} \tag{5}$$

$$h_{VB}^+ + RhB \rightarrow \text{degradation products} \tag{6}$$

$$O_2 + 2e_{CB}^- \rightarrow {}^{\cdot}O_2^- \tag{7}$$

$${}^{\cdot}O_2^- + RhB \rightarrow \text{degradation products} \tag{8}$$

The high photo-activity is synergistically attributed to the ameliorative electronic structure, improved lateral charge transport and interlayer exciton dissociation. For the hydrogen evolution process, the CNUS with a sub band gap (2.37 eV) extends the visible-light absorption region up near to 800 nm. As shown in Eqs. (1)–(3), the excited electrons (e_{CB}^-) on the conduction band will transfer to the surface of the photocatalyst, while the holes (h_{VB}^+) remain on the valence band. With the simultaneous enhancements in π-π* and n-π* electron transitions, the narrowed stacking distance leads to photo-excited electron-hole pairs in the interior of CNUS rapidly transferring to the surface of co-catalyst Pt and then participating reactions. Meanwhile, it is easy for the sacrificial triethanolamine (TEOA) molecules in the reaction solution get access to the abundant adsorption centers on the surface, and then producing oxidative products (Ox).

Usually, the photodegradation of RhB is highly related to the cleavage of the conjugated chromophore, and this process has a deep relationship with the resolved oxygen [72]. According to the results of XPS, the presence of S—C and C—O owing to substitution of S to N sites in carbon nitrogen structure are benefiting to the photocatalytic performance for both hydrogen generation and RhB degradation [73]. According to performance of CNUS, we make a conclusion that the doping of oxygen and sulfur is important for the photocatalytic process in our case. Notably, the VB potential of CNU (+ 1.71 eV) and CNUS (+ 1.61 eV) is lower than the standard redox potential of $OH^-/{}^{\cdot}OH$ (1.99 eV vs NHE, pH = 7) [47]. Thus, it is reasonable that the OH^- anion cannot be oxidized to ${}^{\cdot}OH$ by h_{VB}^+. Due to the more positive redox potential of $O_2/{}^{\cdot}O_2^-$ (−0.046 eV) [26] than the CB edge potential of CNU (−1.26 eV) and CNUS (−1.35 eV), especially, for the midgap energy level of CNUS at −0.76 eV, the separated electrons (e_{CB}^-) on the surface can reduce the dissolved O_2 in the aqueous solution into highly active ${}^{\cdot}O_2^-$, as shown in Eq. (7). It is clear that the existence of midgap band energy for CNUS is another promoted factor for the reduction process. On the basis of the above discussion, it is expected that the ${}^{\cdot}OH$ radicals act as a minor role in the photodegradation of RhB as confirmed by the trapping and ESR/DMPO experiments. As shown in Fig. 4h, the characteristic peaks of DMPO-${}^{\cdot}O_2^-$ are detected in the methanol dispersion under visible light irradiation

while no such signals are observed in dark conditions. This indicates that the photogenerated electrons can be transformed into ${}^{\cdot}O_2^-$ radicals during the photodegradation process, as shown in Eq. (7). However, as seen in Fig. 4i, the characteristic peaks of DMPO-${}^{\cdot}OH$ cannot be observed under visible light irradiation, which is agreed with the trapping experiments and further confirmed that ${}^{\cdot}O_2^-$ active species are formed during the photocatalytic process. Moreover, the intensity for the signal of DMPO-${}^{\cdot}O_2^-$ in the CNUS was much stronger than that in the CNU, which is consistent with the higher RhB degradation in the CNUS photocatalyst [74–76]. This might be caused by the high separation of photo-generated holes-electrons in this distorted structure. Therefore, we can conclude that both hydrogen generation and RhB degradation are strongly relied on the rapidly separated electrons which can be achieved in our distorted structure. Therefore, the mainly promoted effects on photo-activities are coming from the distorted structure and vacancies. According to the active species capture studies, the main active substance is ${}^{\cdot}O_2^-$, and the secondary active substance is h^+.

A possible mechanistic proposal for the photocatalytic process over CNUS photocatalyst is given in Fig. 5. Benefitting from the compacted interlayers stacking distance with oxygen impurity, firstly, more visible light can be harvested by the CNUS due to the modification of both electronic structure and texture. In addition, the presence of sub band gap (2.37 eV) in the sample can also retard the recombination of electron-hole pairs and be helpful for the photocatalytic efficiency. The faster separation rate of carriers endows the photo-induced electrons and holes more reactive. As a result, the strong synergetic effects among these characters enhance the photocatalytic activity of hydrogen generation and RhB degradation, which are achieved by our combinative method simultaneously tailoring the electronic, crystal, surface and textural structures.

3. Conclusion

In summary, a novel isopropanol assisted solvothermal-copolymerization strategy (AIP-assisted) method combining solvothermal and copolymerization has been developed to prepare a distorted g-C₃N₄ photocatalyst. The morphological and structural analysis demonstrate that the CNUS is doped with oxygen and sulfur, which are play pivotal role in both the structure of CNUS and photocatalytic activities. Owing to the higher electronegativity of oxygen atoms and the larger atomic radius of S, the meliorative structure not only shrunken the interlayer distance but also outspread n-π* electron transitions, which endows this new photocatalyst with enhanced visible-light absorption, shortened charge-to-surface migration length and improved charge mobility. Therefore, an impressive visible-light photocatalytic H₂-production activity of 109.3 μmol h⁻¹ and RhB degradation rate of 0.12 min⁻¹ are

achieved over the CNUS. Notably, the compacted stacking of interlayers significantly contributes to the whole meliorative optical band gap and electronic properties, and thus enhances the visible-light photoactivity. More importantly, an easy route has been utilized to tail the photo-electrical and physicochemical properties, which may open a new avenue to prepare another metal-free CN-based materials for solar light-driven H_2 generation, contaminant degradation or CO_2 reduction.

4. Experimental section

4.1. Reagent

Urea (CH_4N_2O), thiourea (CH_4N_2S), melamine (MM, $C_3H_6N_6$) and isopropanol (C_3H_8O) was supplied from Sinopharm Chemical Reagent (China). All of the above chemicals were used as purchased without any further purification.

4.2. Preparation of CNU

The CNU was prepared using urea as precursor via one-step thermal polymerization. In a typical synthesis, 10 g urea was calcined at 550 °C in air for 3 h (heating rates: 5 °C /min).

4.3. Preparation of CNM

The CNM was prepared using melamine as precursor via one-step thermal polymerization. In a typical synthesis, 6 g MM was calcined at 550 °C in air for 3 h (heating rates: 5 °C /min).

4.4. Preparation of CNUS

The synthesis of CNUS was carried out as follows: 5 g urea and 5 g thiourea were dissolved in 20 mL isopropanol, and solvothermal-heated to 200 °C for 12 h. Then, the resulting brown transition was heated in a crucible from room temperature to 550 °C in air and kept for 3 h.

4.5. Characterization

The powder X-ray diffraction (XRD) characterization was performed on an X'Pert Pro automatic powder diffractometer operated at 35 kV and 15 mA using CuKa (k = 0.15406 nm) monochromatized radiation in all cases. The nitrogen physisorption was measured with a Micromeritics ASAP 3020 apparatus. The scanning electron microscopy (SEM) images were obtained on Zeiss SIGMA. The transmission electron microscopy (TEM) experiments were performed using an FEI Tecnai 30 high-resolution transmission electron microscope (Philips Analytical). The Fourier transform infrared (FT-IR) spectra were recorded on a Thermo Nicolet Nexus spectrometer. The X-ray photoelectron spectro-scopy (XPS) measurements were made with a Qtac100 spectrometer using the incident radiation Al Ka of 1486.6 eV at 250 W, 20 mA, and 50 eV pass energy. The C 1 s peak at 284.6 eV was used as the internal standard to compensate for the sample charging. The elemental analysis was performed on a Vario EL III elemental analyzer. The electron spin resonance (ESR) measurements were carried out with Bruker ESR300E at room temperature in the air. For detecting the active species, 10.0 mg samples were dissolved in 5 mL deionized water and 5 mL methanol for detecting ·OH and ·$O_2{}^-$, respectively. And then 30 μL 5,5-diemthyl-1-pyrroline *N*-oxide (DMPO) was added with ultrasonic treatment for 5 min. The DMPO spin-trapping ESR spectra for superoxide radical and hydroxyl radical were examined in dark and visible light, respectively.

The diffuse-reflectance UV–vis (DRS) spectra were recorded on a Varian-Cary 5000 spectrometer equipped with a diffuse-reflectance accessory. The spectra were collected with $BaSO_4$ as a reference. The photoluminescence (PL) spectroscopy measurements were performed using a Hitachi F-7000 fluorescence spectrophotometer. The time-re-solved PL decay curves were recorded on a FLS980 fluorescence

lifetime spectrophotometer (Edinburgh Instruments, UK) under the excitation of 377 nm and probed at 535 nm. The electrochemical impedance spectroscopy (EIS) measurements were carried out at −0.4 V (vs. Ag/AgCl) in 0.2 M Na_2SO_4 aqueous solution with a three-electrode configuration, that is made up of a glassy carbon electrode deposited with the photocatalysts as the work electrode, a platinum wire as the counter electrode, and a Ag/AgCl (saturated in KCl solution) as the reference electrode, over the frequency range 0.1–10^6 HZ.

4.6. Photocurrent measurements

The photoelectrochemical (PEC) measurements were performed on an electrochemical system (CHI-660E, China) with a standard three-electrode cell with a working electrode (as-prepared photocatalyst), a platinum wire as counter electrode and a standard calomel electrode (SCE) as reference electrode and a 300 W Xe lamp as the visible light source. 0.2 M Na_2SO_4 aqueous solution was used as the electrolyte. The working electrodes were prepared as follows: 5 mg of the as-prepared photocatalyst was dispersed in 1 mL water, 250 μL isopropanol and 50 μL nafion solution (5 wt %) to produce a slurry, than 10 μL suspen-sion was coated on a 1 cm × 1 cm glassy carbon electrodes at room temperature.

4.7. Photocatalytic reaction

The photocatalytic performance for H_2 generation was carried out in a top-irradiation quartz vessel connected to a glass closed system with a 300 W Xe lamp as the light source with a 420 nm cutoff filter provided visible light irradiation. Before exposure to light irradiation, the reactional system was evacuated with a vacuum pump for 30 min to remove the air in the dark with stirring uninterruptedly. Typically, 30.0 mg photocatalyst was added to an aqueous solution (60.0 mL) of triethanolamine (10 vol %, as a sacrificial reagent). The amount of H_2 evolved was determined using a gas chromatography (GC 2060 system). The photocatalytic activity of all products was examined by the photodegradation of rhodamine B (RhB) under visible-light irra-diation with a 420 nm cutoff filter. Typically, 50 mg photocatalyst was added into 100 mL aqueous solution of RhB (10 mg L^{-1}) in a quartz reactor. Prior to visible-light irradiation, the suspension was magneti-cally stirred in dark for 0.5 h to ensure the adsorption-desorption equilibrium between photocatalyst and RhB. During irradiation, 3 mL dispersion was taken out at different time intervals (10 min), and then centrifuged at 10,000 rpm to remove the photocatalysts. The con-centration of RhB was examined by measuring the absorption intensity at 554 nm using UV2550 spectrometer.

Conflict of interest

The authors declare no competing financial interest.

Appendix A. Supplementary data

Supplementary material related to this article can be found, in the online version, at doi: https://doi.org/10.1016/j.apcatb.2018.09.080.

References

[1] J. Yang, D. Chen, Y. Zhu, Y. Zhang, Y. Zhu, 3D-3D porous Bi_2WO_6/graphene hydrogel composite with excellent synergistic effect of adsorption-enrichment and photocatalytic degradation, Appl. Catal. B: Environ. 205 (2017) 228–237.

[2] W. Wei, D. Liu, Z. Wei, Y. Zhu, Short-range π-π stacking assembly on P25 TiO_2 nanoparticles for enhanced visible-light photocatalysis, ACS Catal. 7 (2016) 652–663.

[3] Q. Li, T. Shi, X. Li, K. Lv, M. Li, F. Liu, H. Li, M. Lei, Remarkable positive effect of Cd $(OH)_2$ on CdS semiconductor for visible-light photocatalytic H_2 production, Appl. Catal. B: Environ. 229 (2018) 8–14.

[4] G. Yang, H. Ding, D. Chen, J. Feng, Q. Hao, Y. Zhu, Construction of urchin-like $ZnIn_2S_4$-Au-TiO_2 heterostructure with enhanced activity for photocatalytic hydrogen evolution, Appl. Catal. B: Environ. 234 (2018) 260–267.

[5] X.C. Wang, K. Maeda, A. Thomas, K. Takanabe, G. Xin, J.M. Carlsson, K. Domen, M. Antonietti, A metal-free polymeric photocatalyst for hydrogen production from water under visible light, Nat. Mater. 8 (2009) 76–80.

[6] P.K. Chuang, K.H. Wu, T.F. Yeh, H. Teng, Extending the π-conjugation of g-C_3N_4 by incorporating aromatic carbon for photocatalytic H_2 evolution from aqueous solution, ACS Sustain, Chem. Eng. 4 (2016) 5989–5997.

[7] Y. Zeng, C. Liu, L. Wang, S. Zhang, Y. Ding, Y. Xu, Y. Liu, S. Luo, A three-dimensional graphitic carbon nitride belt network for enhanced visible light photocatalytic hydrogen evolution, J. Mater. Chem. A 4 (2016) 19003–19010.

[8] L. Yang, J. Huang, L. Shi, L. Cao, Q. Yu, Y. Jie, J. Fei, H. Ouyang, J. Ye, A surface modification resultant thermally oxidized porous g-C_3N_4 with enhanced photocatalytic hydrogen production, Appl. Catal. B: Environ. 204 (2017) 335–345.

[9] J. Lin, Z. Pan, X. Wang, Photochemical reduction of CO2 by graphitic carbon nitride polymers, ACS Sustain Chem. Eng. 2 (2013) 353–358.

[10] R. Kuriki, K. Sekizawa, O. Ishitani, K. Maeda, Visible-light-driven CO_2 reduction with carbon nitride: enhancing the activity of ruthenium catalysts, Angew. Chem. Int. Ed. 54 (2015) 2406–2409.

[11] K. Wang, Q. Li, B. Liu, B. Cheng, W. Ho, J. Yu, Sulfur-doped g-C_3N_4 with enhanced photocatalytic CO_2-reduction performance, Appl. Catal. B: Environ. 176-177 (2015) 44–52.

[12] G. Gao, Y. Jiao, E.R. Waclawik, A. Du, Single atom (Pd/Pt) supported on graphitic carbon nitride as an efficient photocatalyst for visible-light reduction of carbon dioxide, J. Am. Chem. Soc. 138 (2016) 6292–6297.

[13] G. Mamba, A.K. Mishra, Graphitic carbon nitride (g-C_3N_4) nanocomposites: a new and exciting generation of visible light driven photocatalysts for environmental pollution remediation, Appl. Catal. B: Environ. 198 (2016) 347–377.

[14] C. Lu, P. Zhang, S. Jiang, X. Wu, S. Song, M. Zhu, Z. Lou, Z. Li, F. Liu, Y. Liu, Y. Wang, Z. Le, Photocatalytic reduction elimination of UO_2^{2+} pollutant under visible light with metal-free sulfur doped g-C_3N_4 photocatalyst, Appl. Catal. B: Environ. 200 (2017) 378–385.

[15] X. Zhang, X. Xie, H. Wang, J. Zhang, B. Pan, Y. Xie, Enhanced photoresponsive ultrathin graphitic-phase C_3N_4 nanosheets for bioimaging, J. Am. Chem. Soc. 135 (2013) 18–21.

[16] K.S. Lakhi, D.H. Park, K. Al-Bahily, W. Cha, B. Viswanathan, J.H. Choy, A. Vinu, Mesoporous carbon nitrides: synthesis, functionalization, and applications, Chem. Soc. Rev. 46 (2017) 72–101.

[17] W.J. Ong, L.L. Tan, Y.H. Ng, S.T. Yong, S.P. Chai, Graphitic carbon nitride (g-C_3N_4)-based photocatalysts for artificial photosynthesis and environmental remediation: are we a step closer to achieving sustainability? Chem. Rev. 116 (2016) 7159–7329.

[18] Z. Zhao, Y. Sun, F. Dong, Graphitic carbon nitride based nanocomposites: a review, Nanoscale 7 (2015) 15–37.

[19] Q. Liang, Z. Li, Z.H. Huang, F. Kang, Q.H. Yang, Holey graphitic carbon nitride nanosheets with carbon vacancies for highly improved photocatalytic hydrogen production, Adv. Funct. Mater. 25 (2015) 6885–6892.

[20] G. Rubasinghege, V.H. Grassian, Role(s) of adsorbed water in the surface chemistry of environmental interfaces, Chem. Commun. 49 (2013) 3071–3094.

[21] D. Zheng, X.N. Cao, X. Wang, Precise formation of a hollow carbon nitride structure with a janus surface to promote water splitting by photoredox catalysis, Angew. Chem. Int. Ed. 55 (2016) 11512–11516.

[22] S. Guo, Z. Deng, M. Li, B. Jiang, C. Tian, Q. Pan, H. Fu, Phosphorus-doped carbon nitride tubes with a layered micro-nanostructure for enhanced visible-light photocatalytic hydrogen evolution, Angew. Chem. Int. Ed. 55 (2016) 1830–1834.

[23] T. Xiong, W. Cen, Y. Zhang, F. Dong, Bridging the g-C_3N_4 interlayers for enhanced photocatalysis, ACS Catal. 6 (2016) 2462–2472.

[24] M.M. Khan, S.A. Ansari, D. Pradhan, M.O. Ansari, D.H. Han, J. Lee, M.H. Cho, Band gap engineered TiO2 nanoparticles for visible light induced photoelectrochemical and photocatalytic studies, J. Mater. Chem. A 2 (2014) 637–644.

[25] M. Zhu, S. Kim, L. Mao, M. Fujitsuka, J. Zhang, X. Wang, T. Majima, Metal-free photocatalyst for H_2 evolution in visible to near infrared region: black phosphorus/graphitic carbon nitride, J. Am. Chem. Soc. 139 (2017) 13234–13242.

[26] Q. Liang, Z. Li, Y. Bai, Z.H. Huang, F. Kang, Q.H. Yang, A composite polymeric carbon nitride with in situ formed isotype heterojunctions for highly improved photocatalysis under visible light, Small 13 (2017) 1603182.

[27] S. Yang, Y. Gong, J. Zhang, L. Zhan, L. Ma, Z. Fang, R. Vajtai, X. Wang, P.M. Ajayan, Exfoliated graphitic carbon nitride nanosheets as efficient catalysts for hydrogen evolution under visible light, Adv. Mater. 25 (2013) 2452–2456.

[28] Q. Han, B. Wang, Y. Zhao, C. Hu, L.T. Qu, A graphitic-C_3N_4 "seaweed" architecture for enhanced hydrogen evolution, Angew. Chem. Int. Ed. 54 (2015) 11433–11437.

[29] J. Ran, T.Y. Ma, G. Gao, X.W. Du, S.Z. Qiao, Porous P-doped graphitic carbon nitride nanosheets for synergistically enhanced visible-light photocatalytic H_2 production, Energy Environ. Sci. 8 (2015) 3708–3717.

[30] P. Niu, L.C. Yin, Y.Q. Yang, G. Liu, H.M. Cheng, Increasing the visible light absorption of graphitic carbon nitride (melon) photocatalysts by homogeneous self-modification with nitrogen vacancies, Adv. Mater. 26 (2014) 8046–8052.

[31] J. Ding, W. Xu, H. Wan, D. Yuan, C. Chen, L. Wang, G. Guan, W.L. Dai, Nitrogen vacancy engineered graphitic C_3N_4-based polymers for photocatalytic oxidation of aromatic alcohols to aldehydes, Appl. Catal. B: Environ. 221 (2018) 626–634.

[32] W. Che, W. Cheng, T. Yao, F. Tang, W. Liu, H. Su, Y. Huang, Q. Liu, J. Liu, F. Hu, Z. Pan, Z. Sun, S. Wei, Fast photoelectron transfer in (C_{ring})-C_3N_4 plane heterostructural nanosheets for overall water splitting, J. Am. Chem. Soc. 139 (2017) 3021–3026.

[33] D. Zeng, W.J. Ong, H. Zheng, M. Wu, Y. Chen, D.L. Peng, M.Y. Han, $Ni_{12}P5$ nanoparticles embedded into porous g-C_3N_4 nanosheets as a noble-metal-free heterostructure photocatalyst for efficient H_2 production under visible light, J. Mater. Chem. A 5 (2017) 16171–16178.

[34] D. Zeng, W. Xu, W.J. Ong, J. Xu, H. Ren, Y. Chen, H. Zheng, D.L. Peng, Toward noble-metal-free visible-light-driven photocatalytic hydrogen evolution: monodisperse sub-15 nm Ni_2P nanoparticles anchored on porous g-C_3N_4 nanosheets to engineer 0D-2D heterojunction interfaces, Appl. Catal. B: Environ. 221 (2018) 47–55.

[35] J. Wen, J. Xie, H. Zhang, A. Zhang, Y. Liu, X. Chen, X. Li, Constructing multifunctional metallic Ni interface layers in the g-C_3N_4 nanosheets/amorphous NiS heterojunctions for efficient photocatalytic H_2 generation, ACS Appl. Mater. Interfaces 9 (2017) 14031–14042.

[36] J. Wen, J. Xie, Z. Yang, R. Shen, H. Li, X. Luo, X. Chen, X. Li, Fabricating the robust g-C_3N_4 nanosheets/carbons/NiS multiple heterojunctions for enhanced photocatalytic H_2 generation: an insight into the trifunctional roles of nanocarbons, ACS Sustain. Chem. Eng. 5 (2017) 2224–2236.

[37] Y. Zhu, Y. Xu, Y. Hou, Z. Ding, X. Wang, Cobalt sulfide modified graphitic carbon nitride semiconductor for solar hydrogen production, Inter. J. Hydro. Energy 39 (2014) 11873–11879.

[38] F. Guo, W. Shi, H. Wang, M. Han, H. Li, H. Huang, Y. Liu, Z. Kang, Facile fabrication of a CoO/g-C_3N_4 p-n heterojunction with enhanced photocatalytic activity and stability for tetracycline degradation under visible light, Catal. Sci. Technol. 7 (2017) 3325–3331.

[39] Z. Zhuang, Y. Li, Z. Li, F. Lv, Z. Lang, K. Zhao, L. Zhou, L. Moskaleva, S. Guo, L. Mai, MoB/g-C_3N_4 interface materials as a schottky catalyst to boost hydrogen evolution, Angew. Chem. Int. Ed. 57 (2018) 496–500.

[40] D. Zeng, P. Wu, W.J. Ong, B. Tang, M. Wu, H. Zheng, Y. Chen, D.L. Peng, Construction of network-like and flower-like 2H-$MoSe_2$ nanostructures coupled with porous g-C_3N_4 for noble-metal-free photocatalytic H_2 evolution under visible light, Appl. Catal. B: Environ. 233 (2018) 26–34.

[41] Z. Liu, G. Wang, H.S. Chen, P. Yang, An amorphous/crystalline g-C_3N_4 homojunction for visible light photocatalysis reactions with superior activity, Chem. Comm. 54 (2018) 4720–4723.

[42] Y. Chen, B. Wang, S. Lin, Y. Zhang, X.C. Wang, Activation of n→π* Transitions in two-dimensional conjugated polymers for visible light photocatalysis, J. Phys. Chem. C 118 (2014) 29981–29989.

[43] G. Zhang, A. Savateev, Y. Zhao, L. Li, M. Antonietti, Advancing the n→π* electron transition of carbon nitride nanotubes for H_2 photosynthesis, J. Mater. Chem. A 5 (2017) 12723–12728.

[44] G. Zhang, G. Li, Z.A. Lan, L. Lin, A. Savateev, T. Heil, S. Zafeiratos, X. Wang, M. Antonietti, Optimizing optical absorption, exciton dissociation, and charge transfer of a polymeric carbon nitride with ultrahigh solar hydrogen production activity, Angew. Chem. Int. Ed. 56 (2017) 13445–13449.

[45] J. Cheng, Z. Hu, K. Lv, X. Wu, Q. Li, Y. Li, X. Li, J. Sun, Drastic promoting the visible photoreactivity of layered carbon nitride by polymerization of dicyandiamide at high pressure, Appl. Catal. B: Environ. (2018) 330–339.

[46] C. Liu, H. Huang, W. Cui, F. Dong, Y. Zhang, Band structure engineering and efficient charge transport in oxygen substituted g-C_3N_4 for superior photocatalytic hydrogen evolution, Appl. Catal. B: Environ. 230 (2018) 115–124.

[47] M. Jourshabani, Z. Shariatinia, A. Badiei, Controllable synthesis of mesoporous sulfur-doped carbon nitride materials for enhanced visible light photocatalytic degradation, Langmuir 33 (2017) 7062–7078.

[48] J. Zhang, M. Zhang, G. Zhang, X. Wang, Synthesis of carbon nitride semiconductors in sulfur flux for water photoredox catalysis, ACS Catal. 2 (2012) 940–948.

[49] F. Wei, Y. Liu, H. Zhao, X. Ren, J. Liu, T. Hasan, L. Chen, Y. Li, B.L. Su, Oxygen self-doped g-C_3N_4 with tunable electronic band structure for unprecedentedly enhanced photocatalytic performance, Nanoscale 10 (2018) 4515–4522.

[50] D. Masih, Y. Ma, S. Rohani, Graphitic C_3N_4 based noble-metal-free photocatalyst systems: a review, Appl. Catal. B: Environ. 206 (2017) 556–588.

[51] Y. Zeng, X. Liu, C. Liu, L. Wang, Y. Xia, S. Zhang, S. Luo, Y. Pei, Scalable one-step production of porous oxygen-doped g-C_3N_4 nanorods with effective electron separation for excellent visible-light photocatalytic activity, Appl. Catal. B: Environ. 224 (2018) 1–9.

[52] D. Zhang, Y. Guo, Z. Zhao, Porous defect-modified graphitic carbon nitride via a facile one-step approach with significantly enhanced photocatalytic hydrogen evolution under visible light irradiation, Appl. Catal. B: Environ. 226 (2018) 1–9.

[53] X.C. Wang, K. Maeda, X.F. Chen, K. Takanabe, K. Domen, Y.D. Hou, M. Antonietti, Polymer semiconductors for artificial photosynthesis: hydrogen evolution by mesoporous graphitic carbon nitride with visible light, J. Am. Chem. Soc. 131 (2009) 1680–1681.

[54] S. Cao, J. Low, J. Yu, M. Jaroniec, Polymeric photocatalysts based on graphitic carbon nitride, Adv. Mater. 27 (2015) 2150–2176.

[55] X. Dong, F. Cheng, Recent development in exfoliated two-dimensional g-C3N4 nanosheets for photocatalytic applications, J. Mater. Chem. A 3 (2015) 23642–23652.

[56] Y. Kofuji, Y. Isobe, Y. Shiraishi, H. Sakamoto, S. Tanaka, S. Ichikawa, T. Hirai,

Carbon nitride-aromatic diimide-graphene nanohybrids: metal-free photocatalysts for solar-to-hydrogen peroxide energy conversion with 0.2 % efficiency, J. Am. Chem. Soc. 138 (2016) 10019–10025.

[57] J. Tian, Q. Liu, C. Ge, Z. Xing, A.M. Asiri, A.O. Al-Youbi, X. Sun, Ultrathin graphitic carbon nitride nanosheets: a low-cost, green, and highly efficient electrocatalyst toward the reduction of hydrogen peroxide and its glucose biosensing application, Nanoscale 5 (2013) 8921–8924.

[58] J. Zhang, X. Chen, K. Takanabe, K. Maeda, K. Domen, J.D. Epping, X. Fu, M. Antonietti, X. Wang, Synthesis of a carbon nitride structure for visible-light catalysis by copolymerization, Angew. Chem. Int. Ed. 49 (2010) 441–444.

[59] D.J. Martin, P.J. Reardon, S.J. Moniz, J. Tang, Visible light-driven pure water splitting by a nature-inspired organic semiconductor-based system, J. Am. Chem. Soc. 136 (2014) 12568–12571.

[60] Y. Li, M. Yang, Y. Xing, X. Liu, Y. Yang, X. Wang, S. Song, Preparation of carbon-rich g-C$_3$N$_4$ nanosheets with enhanced visible light utilization for efficient photocatalytic hydrogen production, Small 13 (2017) 1701552.

[61] L. Shi, L. Yang, W. Zhou, Y. Liu, L. Yin, X. Hai, H. Song, J. Ye, Photoassisted construction of holey defective g-C$_3$N$_4$ photocatalysts for efficient visible-light-driven H$_2$O$_2$ production, Small 14 (2018) 1703142.

[62] C. Liu, Y. Zhang, F. Dong, A.H. Reshak, L. Ye, N. Pinna, C. Zeng, T. Zhang, H. Huang, Chlorine intercalation in graphitic carbon nitride for efficient photocatalysis, Appl. Catal. B: Environ. 203 (2017) 465–474.

[63] P. Dong, B. Yang, C. Liu, F. Xu, X. Xi, G. Hou, R. Shao, Highly enhanced photocatalytic activity of WO$_3$ thin films loaded with Pt–Ag bimetallic alloy nanoparticles, RSC Adv. 7 (2017) 947–956.

[64] P. Dong, G. Hou, C. Liu, X. Zhang, H. Tian, F. Xu, X. Xi, R. Shao, Origin of activity and stability enhancement for Ag$_3$PO4 photocatalyst after calcination, Materials 9 (2016) 968.

[65] H. Yaghoubi, Z. Li, Y. Chen, H.T. Ngo, V.R. Bhethanabotla, B. Joseph, S. Ma, R. Schlaf, A. Takshi, Toward a visible light-driven photocatalyst: the effect of midgap-states-induced energy gap of undoped TiO$_2$ nanoparticles, ACS Catal. 5 (2014) 327–335.

[66] J. Zhang, S. Liu, J. Yu, M. Jaroniec, A simple cation exchange approach to Bi-doped ZnS hollow spheres with enhanced UV and visible-light photocatalytic H$_2$-production activity, J. Mater. Chem. 21 (2011) 14655–14662.

[67] G. Zhang, X. Wang, A facile synthesis of covalent carbon nitride photocatalysts by Co-polymerization of urea and phenylurea for hydrogen evolution, J. Catal. 307 (2013) 246–253.

[68] J. Zhang, M. Zhang, S. Lin, X. Fu, X. Wang, Molecular doping of carbon nitride photocatalysts with tunable bandgap and enhanced activity, J. Catal. 310 (2014) 24–30.

[69] S. Cao, H. Li, T. Tong, H.C. Chen, A. Yu, J. Yu, H.M. Chen, Single-atom engineering of directional charge transfer channels and active sites for photocatalytic hydrogen evolution, Adv. Funct. Mater. (2018) 1802169.

[70] J. Ran, J. Zhang, J. Yu, M. Jaroniec, S.Z. Qiao, Earth-abundant cocatalysts for semiconductor-based photocatalytic water splitting, Chem. Soc. Rev. 43 (2014) 7787–7812.

[71] A. Kudo, Y. Miseki, Heterogeneous photocatalyst materials for water splitting, Chem. Soc. Rev. 38 (2009) 253–278.

[72] Q. Guo, Y. Zhang, H.S. Zhang, Y. Liu, Y.J. Zhao, J. Qiu, G. Dong, 3D foam strutted graphene carbon nitride with highly stable optoelectronic properties, Adv. Funct. Mater. 27 (2017) 1703711.

[73] P.N. Gang Liu, C.H. Sun, S.C. Smith, Z.G. Chen, G.Q. Lu, H.M. Cheng, Unique electronic structure induced high photoreactivity of sulfur-doped graphitic C$_3$N$_4$, J. Am. Chem. Soc. 132 (2010) 11642–11648.

[74] C. Liu, Q. Wu, M. Ji, H. Zhu, H. Hou, Q. Yang, C. Jiang, J. Wang, L. Tian, J. Chen, W. Hou, Constructing Z-scheme charge separation in 2D layered porous BiOBr/graphitic C$_3$N$_4$ nanosheets nanojunction with enhanced photocatalytic activity, J. Alloy. Comp. 723 (2017) 1121–1131.

[75] Y. Wang, W. Jiang, W. Luo, X. Chen, Y. Zhu, Ultrathin nanosheets g-C$_3$N$_4$ @Bi$_2$WO$_6$ core-shell structure via low temperature reassembled strategy to promote photocatalytic activity, Appl. Catal. B: Environ. 237 (2018) 633–640.

[76] C. Liu, H. Zhu, Y. Zhu, P. Dong, H. Hou, Q. Xu, X. Chen, X. Xi, W. Hou, Ordered layered N-doped KTiNbO$_5$/g-C$_3$N$_4$ heterojunction with enhanced visible light photocatalytic activity, Appl. Catal. B: Environ. 228 (2018) 54–63.